

EM-Aware Physical Synthesis: Neural Inductor Modeling and Intelligent Placement & Routing for RF Circuits

Yilun Huang[†], Asal Mehradfar^{*}, Salman Avestimehr^{*}, Hamidreza Aghasi[†]

^{*}Electrical Engineering, University of Southern California, Los Angeles, CA, USA

[†]Electrical Engineering and Computer Science, University of California Irvine, Irvine, CA, USA

Abstract—This paper presents an ML-driven framework for automated RF physical synthesis that transforms circuit netlists into manufacturable GDSII layouts. While recent ML approaches demonstrate success in topology selection and parameter optimization, they fail to produce manufacturable layouts due to oversimplified component models and lack of routing capabilities. Our framework addresses these limitations through three key innovations: (1) a neural network framework trained on 18,210 inductor geometries with frequency sweeps from 1–100 GHz, generating 7.5 million training samples that predicts inductor Q-factor with $<2\%$ error and enables fast gradient-based layout optimization with a 93.77% success rate in producing high-Q layouts (2) an intelligent P-Cell optimizer that reduces layout area while maintaining design-rule-check (DRC) compliance, and (3) a complete placement and routing engine with frequency-dependent EM spacing rules and DRC-aware synthesis. The neural inductor model demonstrates superior accuracy across 1–100 GHz, enabling EM-accurate component synthesis with real-time inference. The framework successfully generates DRC-aware GDSII layouts for RF circuits, representing a significant step toward automated RF physical design.

Index Terms—Analog circuit synthesis, electromagnetic modeling, inductor optimization, layout automation, machine learning, millimeter-wave circuits, placement and routing, RF integrated circuits, AI-assisted analog circuit design, neural network

I. INTRODUCTION

The design of analog and radio frequency (RF) circuits remains a critical bottleneck in integrated circuit development, with design cycles often spanning months and requiring extensive expert iteration. The complexity arises from continuous parameter spaces, tight coupling between circuit performance and physical layout, and frequency-dependent electromagnetic effects that dominate behavior at millimeter-wave frequencies. Designers must manually adjust component values, run electromagnetic (EM) simulations, and iterate layout to meet specifications—a process that involves repeated cycles of schematic optimization, layout implementation, and parasitic extraction, creating a fundamental scalability challenge for communications, radar [1], and sensing applications.

Recent advances in machine learning, including evolutionary and surrogate-based methods [2–5], have demonstrated promise for automating circuit design at the schematic level. Frameworks like FALCON [6] achieve high accuracy in topology selection and parameter optimization through neural networks and differentiable optimization [7–9]. Other approaches, including genetic programming, diffusion models, and LLM-based

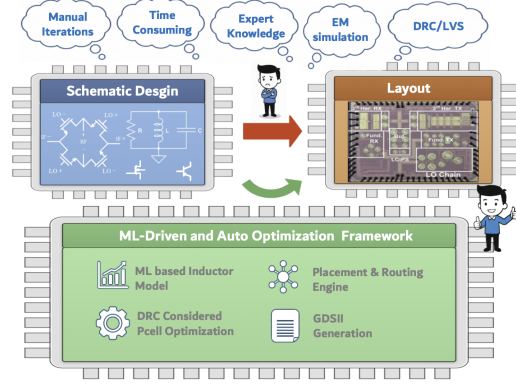


Fig. 1. Proposed RF synthesis framework for automated netlist-to-GDSII.

methods [10–12], explore reinforcement learning for circuit sizing [13, 14] and Bayesian optimization for performance prediction [15]. These methods successfully address the schematic-level optimization problem, generating component values that meet electrical specifications. However, they face a critical limitation: the inability to generate physical layouts required for fabrication. The physical implementation gap poses severe practical challenges. While FALCON effectively introduces layout awareness through differentiable cost functions and achieves good accuracy at RF and low-mm-wave frequencies, its analytical passive models become less reliable at higher mm-wave bands where full electromagnetic effects dominate. Traditional analytical inductor models such as Wheeler's approximation [16] and modified current sheet methods [17] produce Q-factor errors at millimeter-wave frequencies, limiting the accuracy of layout-aware optimization when using these simplified approaches. Furthermore, existing ML frameworks output only optimized component parameters without generating the placement, routing, or GDSII files [18, 19], forcing designers to manually translate these into layouts.

This work bridges ML-based circuit optimization and manufacturable physical layouts through a complete RF synthesis framework in Fig. 1. By replacing inaccurate analytical models with data-driven EM predictions and automating the entire layout generation process, we enable direct netlist-to-GDSII synthesis. The framework makes three key contributions: (1) EM-accurate ML inductor modeling, (2) EM-aware placement and routing and (3) complete netlist-to-GDSII. The framework is validated on 22-nm CMOS RF circuits operating from 1–100 GHz, demonstrating the first complete path from circuit netlist to layout using ML-driven component modeling.

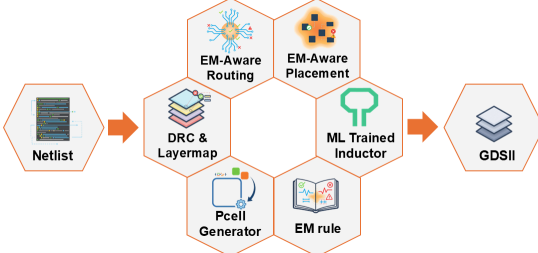


Fig. 2. The proposed pipeline of GDS from netlist generation which captures various types of constraints without an specific order.

II. SYSTEM OVERVIEW

The proposed framework transforms circuit netlists into manufacturable GDSII layouts through an integrated synthesis pipeline, as illustrated in Fig. 2. Beginning with a circuit netlist specification, the framework generates complete physical implementations by orchestrating multiple specialized synthesis engines with electromagnetic awareness.

The **ML-trained Inductor** model addresses the fundamental limitation of analytical inductor equations by leveraging data-driven predictions derived from full-wave electromagnetic simulations. This approach enables accurate inductor synthesis across the 1–100 GHz frequency range, capturing frequency-dependent substrate losses, skin effect, and parasitic coupling that analytical models fail to represent.

Component instantiation for capacitors and resistors is handled by the **PCell Generator**, which systematically explores metal stack configurations to minimize layout area while satisfying electrical specifications and maintaining DRC.

The **EM-aware Placement** engine positions components according to spacing constraints encoded in the **EM Rule** database. These rules implement frequency-dependent minimum separation requirements that mitigate performance degradation arising from substrate coupling and electromagnetic interference—effects that become critical at mm-wave.

Interconnect synthesis is performed by the **EM-aware Routing** engine, which consults both the foundry-specific **Technology Layermap** for appropriate layer assignments and **DRC** constraints for design rule compliance. The routing algorithm incorporates spacing margins to reduce violations that would otherwise necessitate manual layout iteration.

The final **Generator** module assembles component geometries and routing topologies into hierarchical GDSII files.

III. ML-BASED Q-FACTOR PREDICTION AND LAYOUT OPTIMIZATION

A. Data Preprocessing

The dataset used in this study comprises approximately 7.5 million samples, each annotated with a set of geometric and electrical parameters along with the corresponding quality factor (Q). The available parameters include the target specifications (f, W, L) and layout-related variables (L_v, L_h, L_{CN}), where W, L_v, L_h , and L_{CN} denote the inductor width and layout dimensions (all expressed in μm), as illustrated in Fig. 3. L is the inductance in pH, and f is the target frequency in GHz.

Feature Selection and Cleaning. Raw simulation files were parsed to extract $f, W, L, L_v, L_h, L_{CN}$, and Q . Entries with

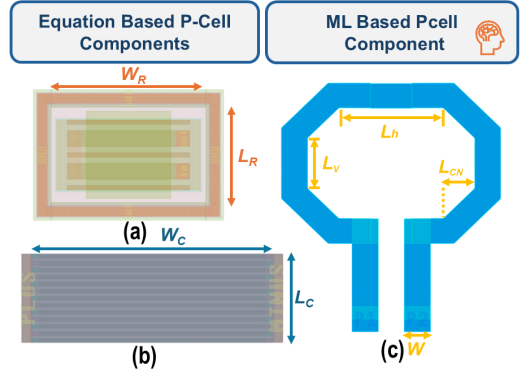


Fig. 3. (a) N+ Diffusion Resistor (b) Analog Passive Metal-Oxide-Metal Capacitor (c) ML Based Inductor

non-physical values were removed, and the cleaned data were aggregated into a unified dataset.

Distribution Visualization. Fig. 4 shows the Q distribution, spanning 0–50 with annotated mean and standard deviation.

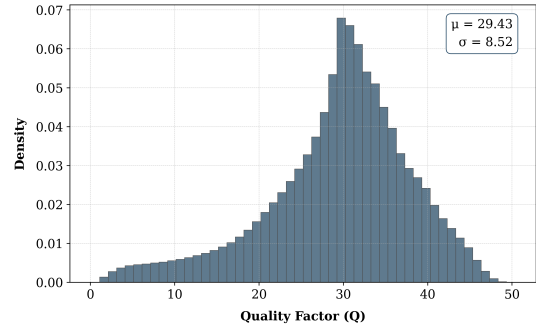


Fig. 4. Distribution of the inductor quality factor Q across the dataset.

Normalization. Design and layout variables ($f, W, L, L_v, L_h, L_{CN}$) were normalized using training-set statistics as $x'_i = (x_i - \mu_i)/\sigma_i$, where μ_i and σ_i are the feature mean and standard deviation. The quality factor Q was left unnormalized to retain physical interpretability.

Data Splitting. The dataset was divided into training, validation, and test sets (80:10:10) using a fixed seed. These subsets were used for learning, hyperparameter tuning, and final evaluation, respectively.

B. Forward Model Training and Evaluation

We formulate quality-factor prediction as a supervised regression task. Given inputs $\mathbf{x} = (f, W, L, L_v, L_h, L_{CN})$, the goal is to learn $Q_\theta(\mathbf{x})$, parameterized by θ , that predicts the corresponding quality factor Q . The model minimizes the mean squared error (MSE), $\mathcal{L}_{\text{MSE}} = \frac{1}{N} \sum_{i=1}^N (Q_\theta(\mathbf{x}_i) - Q_i)^2$, where N is the number of samples and Q_i is the ground-truth label. An MLP model Q_θ is designed with ten hidden layers of widths $\{256, 256, 256, 128, 128, 128, 64, 64, 64, 32\}$, each followed by ReLU and LayerNorm for stability. A final linear layer with Softplus activation, $\text{Softplus}(z) = \log(1 + e^z)$, ensures non-negative outputs consistency with physical constraints.

Training uses Adam (learning rate 0.001, batch size 16,384) with ReduceLROnPlateau to lower the rate when validation

loss plateaus. The model trains for up to 300 epochs with early stopping, and the checkpoint with the lowest validation MSE is used for final testing.

TABLE I
EVALUATION OF FORWARD Q PREDICTION ON HELD-OUT TEST SET.

Metric	Value
Mean Absolute Error (MAE)	0.419
Mean Squared Error (MSE)	0.423
Root Mean Squared Error (RMSE)	0.65
R-squared (R^2 Score)	0.994
Mean Absolute Percentage Error (MAPE)	1.36%

The trained model achieves the results in Table I on the held-out test set, reflecting the prediction error between the model's forward estimates and the actual simulated Q values without any layout optimization. This strong agreement confirms that the model captures the relationship between design parameters and Q , providing a solid foundation for inverse design.

C. Inverse Layout Design via Gradient Reasoning

We adopt a differentiable inverse design strategy inspired by the gradient reasoning method proposed in FALCON [6] to maximize the quality factor Q by tuning layout parameters. Given fixed target specifications—operating frequency f , width W , and inductance L —our goal is to optimize the layout variables: vertical length L_v , horizontal length L_h , and center length L_{CN} . The inverse design task is formulated as $(L_v^*, L_h^*, L_{CN}^*) = \arg \max_{L_v, L_h, L_{CN}} Q_\theta(f, W, L, L_v, L_h, L_{CN})$, where Q_θ denotes the frozen prediction model trained in the forward regression task. The optimization is subject to physical box constraints: $W+2 \leq L_v \leq 100$ (μm), $2W+4 \leq L_h \leq 100$ (μm), and $1 \leq L_{CN} \leq 50$ (μm).

We initialize each optimization run from a feasible design starting point of $(L_v, L_h, L_{CN}) = (40, 40, 20)$ μm . At every step, the candidate values are concatenated with fixed (f, W, L) and normalized using the same training-set statistics used during forward modeling. The normalized vector is passed to the frozen MLP to produce the predicted Q , and the loss function is defined as the negative prediction, $\mathcal{L} = -Q_\theta(f, W, L, L_v, L_h, L_{CN})$.

We use the Adam optimizer with a learning rate of 0.01 to iteratively update (L_v, L_h, L_{CN}) , treating them as differentiable parameters. To enforce layout validity and manufacturability, we clamp these variables to their valid physical ranges after each update. By default, we perform optimization for 3000 steps; however, the stopping criterion is user-configurable—for example, optimization may be terminated early if a target threshold for Q is reached. Importantly, these optimization settings can be modified at inference time without retraining the model, allowing flexible adaptation to diverse design objectives.

To reduce EM simulation cost, inverse design performance is evaluated on 1000 randomly selected samples from the held-out test set. Rather than relying solely on regression metrics, we assess the *success rate*, defined as the percentage of cases where the simulated quality factor Q exceeds a practical threshold. Using $Q > 10$ as the design goal, the method achieves a success rate of 93.77%, indicating that

the learned optimization strategy consistently generates high-performing, physically valid layouts. Each optimization instance runs in under one second on a standard MacBook CPU, showcasing the method's computational efficiency and real-world deployability. The source code is available at: <https://github.com/AsalMehradfar/InductorModeling>

IV. LAYOUT GENERATION

A. Intelligent PCell Optimization

Foundry PCells prioritize flexibility over area. We perform automated search to minimize area while meeting electrical targets and DRC margins.

MOM Capacitor. We use density model $C_{\text{pF}} = \rho_{\text{stack}} A_{\text{eff}} \times 10^{-3}$, where ρ_{stack} is the capacitance density ($\text{fF}/\mu\text{m}^2$) for a specific metal stack configuration and $A_{\text{eff}} = W \cdot L$. For 22 nm CMOS at 1.8 V, stacks span ≥ 3 layers. Given C_{target} , the optimizer enumerates stack choices and (W, L) pairs ($1.0 \leq L \leq 60.0 \mu\text{m}$, $1.0 \leq W \leq 330.0 \mu\text{m}$), selecting minimum-area solution within $\pm 0.5\%$ of target.

Resistor. For poly resistors we model $R_{\text{stripe}} = R_s(L/W) + 2R_{\text{end}}/W$ with R_s (sheet resistance) and R_{end} (contact resistance) based on PDK values. Series/parallel tiling yields $R_{\text{total}} = (N_s/N_p)R_{\text{stripe}}$. We search $1 \leq N_s, N_p \leq 64$ under $0.36 \leq W \leq 3.72 \mu\text{m}$ and $0.40 \leq L \leq 50.0 \mu\text{m}$, choosing smallest-area design meeting target.

B. Multi-Objective Placement Optimization

We optimize device positions $\mathbf{p} = \{(x_i, y_i, \theta_i)\}_{i=1}^N$ where (x_i, y_i) is the coordinate and $\theta_i \in \{0^\circ, 90^\circ, 180^\circ, 270^\circ\}$ is rotation:

$$\min_{\mathbf{p}} C(\mathbf{p}) = \text{HPWL}(\mathbf{p}) + K \sum_{1 \leq i < j \leq N} A_{\text{overlap}}(B_i, B_j), \quad (1)$$

where HPWL (half-perimeter wirelength) measures interconnect length, B_i are device bounding boxes, and $K = 10^4$ penalizes overlaps.

Algorithm 1 Multi-Objective Device Placement

Require: Devices \mathcal{D} , netlist \mathcal{G} , spacing $S_{\min}(f)$, guard Δ
Ensure: Placement \mathbf{p}

- 1: Order by connectivity $d_i = |\{n : i \in P_n\}|$; initial row placement
- 2: **for** $t = 1$ to T_{\max} **do** \triangleright Local search
- 3: Move: swap/translate; $C(\mathbf{p}) = \text{HPWL} + K \sum A_{\text{overlap}}$
- 4: Accept if $C_{\text{new}} < C_{\text{curr}}$, else revert
- 5: **end for**
- 6: **for** each device i **do** \triangleright Rotation
- 7: Score $\theta \in \{0^\circ, 90^\circ, 180^\circ, 270^\circ\}$: $S_\theta = \min_p \max_d (L_{\text{free}} - L_{\text{need}})$
- 8: Select $\theta_i^* = \arg \max S_\theta$
- 9: **end for**

Devices are ordered by connectivity degree d_i . We perform adjacent swaps (exchanging neighboring devices) and small translations, as shown in Fig. 5(a). A move is accepted only if cost improves, considering criticality-weighted HPWL (high-priority nets weighted by $w_n \geq 1$) and soft penalties for tight spacing. All spacings use 10–20% DRC guard-band Δ (heuristically $\sim 10 \mu\text{m}$ at $< 5 \text{ GHz}$, $\sim 30 \mu\text{m}$ at $> 40 \text{ GHz}$). For rotation, we score by $S_\theta = \min_{p \in \text{pins}} \max_{d \in D_p} (L_{\text{free}} - L_{\text{need}})$, where $L_{\text{free}}(p, d, \theta)$ is available routing space from pin p in direction $d \in \{L, R, U, D\}$ (left/right/up/down) at rotation θ , and $L_{\text{need}} = \text{dist}(p, \partial B) + m_{\text{margin}}$ is required escape distance from device boundary ∂B plus margin. NMOS pins (Gate/Drain/Source) are recognized, preferring vertical S/D escapes.

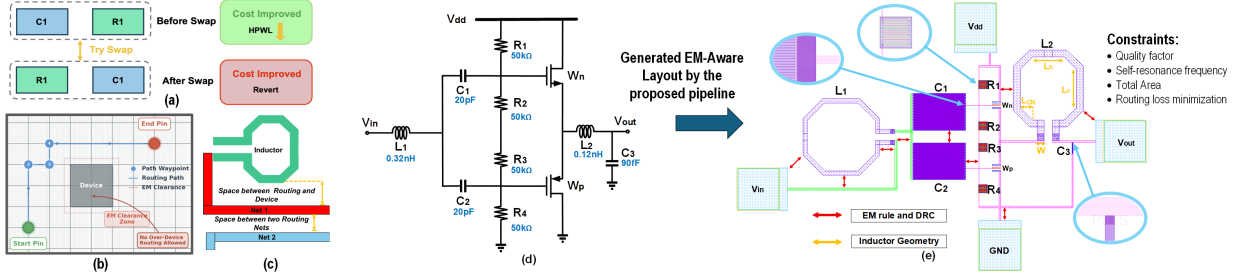


Fig. 5. (a) Adjacent-swap local move. Swap accepted only if augmented objective (criticality-weighted HPWL plus soft separation) improves. (b) Grid-based A* routing on $0.1 \mu\text{m}$ grid avoiding device obstacles with Manhattan routing. (c) Router spacing policy. Top: routing-to-device isolation (no over-cell). Bottom: inter-net spacing. Both obey frequency-aware targets. (d) Designed Class-B PA schematic (e) Generated layout of Class-B PA by the proposed pipeline.

C. Constraint-Driven Global Routing

Routing uses A* on grid $\mathcal{G} = \{(x, y, \ell) : x, y \in 0.1 \mu\text{m}, \ell \in \{\text{M1, QA, QB}\}\}$ where (x, y) are coordinates with $0.1 \mu\text{m}$ resolution and ℓ is the metal layer, with cost function:

$$f(p) = g(p) + h(p) + \lambda_{\text{layer}} \cdot \mathbb{1}_{[\text{layer switch}]}, \quad (2)$$

where $g(p)$ is path cost from start, $h(p) = \|p - t\|_1$ is Manhattan distance to target t , and $\lambda_{\text{layer}} = 10 \cdot g$ discourages vias. Net topology is minimum spanning tree (MST) minimizing $\sum_{e \in E_n} \|e\|_1$. Fig. 5(b) illustrates grid-based routing with obstacle avoidance.

Algorithm 2 EM-Aware A* Global Routing

Require: Pins \mathcal{P}_n , grid \mathcal{G} , layers \mathcal{L} , devices $\{B_i\}$, DRC

Ensure: Routes \mathcal{R}_n

```

1:  $T_n \leftarrow \text{MST}(\mathcal{P}_n)$ ; for each edge  $(s, t) \in T_n$ :
2:    $Q \leftarrow \{(f(s), s)\}$  (min-heap on  $f$ ),  $C \leftarrow \emptyset$ ,  $g(s) \leftarrow 0$ ; step  $h = 0.1 \mu\text{m}$ 
3: while  $Q \neq \emptyset$  do
4:   pop best  $p$  from  $Q$ ; if  $\|p - t\|_1 < h$  then emit path  $\rightarrow$  GDSII; continue
5:   add  $p$  to  $C$ 
6:   for  $d \in \{L, R, U, D\}$  do ▷ in-plane moves
7:      $p' \leftarrow p + h \cdot d$ ; if  $p' \in C$  or DRC-violate( $p'$ ) then continue
8:      $g' \leftarrow g(p) + h$ ;  $f' \leftarrow g' + \|p' - t\|_1$ ; relax/insert  $(f', p')$  into  $Q$ 
9:   end for
10:  for  $\ell' \in \mathcal{L} \setminus \{\ell\}$  do ▷ via moves
11:     $p_v \leftarrow (x, y, \ell')$ ;  $g' \leftarrow g(p) + 10g(p)$ ;  $f' \leftarrow g' + \|p_v - t\|_1$ ; relax/insert
         $(f', p_v)$  into  $Q$ 
12:  end for
13: end while

```

No-over-cell. Expanded segments $R_{\text{seg}} \oplus \mathcal{B}(s_{\text{same}}/2)$ must satisfy $R_{\text{seg}}^{\text{exp}} \cap B_i = \emptyset, \forall i$, except pin corridors along $d \in \{L, R, U, D\}$.

EM-aware spacing. Devices and routes are dilated by required clearance (Fig. 5(c)); grid cells inside halos are blocked. Clearances distinguish routing-to-device (no-over-cell) vs. inter-net spacing (crosstalk prevention) and scale with frequency. All rules use 10–20% guard-bands.

Pin escape. Two-phase: (1) straight escape selecting $d^* = \arg \max_d L_{\text{free}}(p, d)$ with maximum free run, or (2) dogleg (orthogonal-then-primary) if blocked. Both validate no-over-cell and spacing constraints.

D. GDSII Generation

The framework generates hierarchical GDSII files through Python-based PCell assembly using the `gdstk` library, interfacing with foundry PDKs. Notably, in the Class-B PA design example (Fig. 5(d, e)), transistors are represented as simplified three-pin boxes instead of transistor layouts. This simplification

TABLE II
COMPARISON OF THIS WORK WITH PRIOR WORKS: FOCUS ON LAYOUT AND EM AUTOMATION CAPABILITIES

Method	Layout Gen.	EM-Aware	RF/mm-W	Foundry PDK	Public D/C
CktGNN [20]	✗	✗	✗	✗	✓/✓
LaMAGIC [21]	✗	✗	✗	✗	✗/✗
AnalogCoder [22]	✗	✗	✗	✗	✓/✓
GCN-RL [14]	✗	✗	✗	✓	✗/✗
Cao et al. [23]	✗	✗	✗	✓	✗/✗
BO-SPGP [15]	✗	✗	✗	✓	✗/✗
AICircuit [24]	✗	✗	✓	✓	✓/✓
Krylov et al. [25]	✗	✗	✗	✗	✓/✓
LayoutCopilot [26]	✓	✗	✗	✓	✗/✗
AutoCkt [13]	✗	✗	✗	✓	✗/✗
CAN-RL [27]	✓	✗	✗	✓	✗/✗
This Work	✓	✓	✓	✓	✓/✓

Layout Gen.: Automated layout synthesis. *EM-Aware:* EM effects in layout. *RF/mm-W:* RF/mm-wave layout. *Foundry PDK:* Uses foundry PDKs. *Public D/C:* Dataset/Code (format: Data/Code).

represents a current limitation, as the framework does not yet fully support the complex mirroring and symmetry requirements inherent to RF/analog transistor layout design.

V. CONCLUSION

This work presents an EM-aware, ML-driven physical-synthesis flow that maps RF netlists directly to GDSII. A neural inductor surrogate trained on HFSS simulations achieves $<2\%$ Q-factor error across 1–100 GHz inference and enables fast gradient-based layout optimization with a 93.77% success rate of high-Q layouts, enabling EM-accurate passive synthesis. An intelligent PCell optimizer reduces passive area, and a frequency-aware placement-and-routing engine enforces technology rules and spacing to yield hierarchical, DRC-compliant layouts in a 22 nm CMOS process. Next, we will broaden coverage across circuit blocks and technology nodes, strengthen EM-in-the-loop cost modeling and post-layout verification, and enhance robustness to variation and reliability, while exploring tighter integration with higher-level design automation and adaptive rule learning—pushing toward a scalable, production-ready path from schematic intent to tapeout.

ACKNOWLEDGMENT

The authors would like to thank Global Foundries for technology access. This project is partially sponsored under National Science Foundation Grant #2443820.

REFERENCES

[1] X. Liu, M. H. Maktoomi, M. Alesheikh, P. Heydari, and H. Aghasi, “A cmos 49–63-ghz phase-locked stepped-chirp fmcw radar transceiver,” *IEEE Journal of Solid-State Circuits*, 2025.

[2] B. Liu, D. Zhao, P. Reynaert, and G. G. E. Gielen, “Synthesis of integrated passive components for high-frequency RF ICs based on evolutionary computation and machine learning techniques,” *IEEE Trans. Comput.-Aided Design Integr. Circuits Syst.*, vol. 30, no. 10, pp. 1458–1468, 2011.

[3] F. Passos, N. Lourenço, E. Roca, R. Martins, R. Castro-López, N. Horta, and F. V. Fernández, “PACOSYT: A passive component synthesis tool based on machine learning and tailored modeling strategies towards optimal RF and mm-wave circuit designs,” *IEEE J. Microw.*, vol. 3, no. 2, pp. 599–613, 2023.

[4] B. Liu, D. Zhao, P. Reynaert, and G. G. E. Gielen, “GASPAD: A general and efficient mm-wave integrated circuit synthesis method based on surrogate model assisted evolutionary algorithm,” *IEEE Trans. Comput.-Aided Design Integr. Circuits Syst.*, vol. 33, no. 2, pp. 169–182, 2014.

[5] A. Mehradfar, X. Zhao, Y. Niu, S. Babakniya, M. Alesheikh, H. Aghasi, and S. Avestimehr, “Supervised Learning for Analog and RF Circuit Design: Benchmarks and Comparative Insights,” *arXiv preprint arXiv:2501.11839*, 2025.

[6] A. Mehradfar, X. Zhao, Y. Huang, E. Ceyani, Y. Yang, S. Han, H. Aghasi, and S. Avestimehr, “FALCON: An ML Framework for Fully Automated Layout-Constrained Analog Circuit Design,” in *The Thirty-ninth Annual Conference on Neural Information Processing Systems*, 2025.

[7] E. A. Karahan, Z. Liu, A. Gupta, Z. Shao, J. Zhou, U. Khankhoe, and K. Sengupta, “Deep-learning enabled generalized inverse design of multi-port radio-frequency and sub-terahertz passives and integrated circuits,” *Nature Commun.*, vol. 15, no. 1, p. 10734, 2024.

[8] J. Zhang, Z. Wei, K. Kang, and W.-Y. Yin, “Intelligent inverse designs of impedance matching circuits with generative adversarial network,” *IEEE Trans. Comput.-Aided Design Integr. Circuits Syst.*, vol. 43, no. 10, pp. 3171–3183, 2024.

[9] L.-Y. Xiao, W. Shao, F.-L. Jin, B.-Z. Wang, and Q. H. Liu, “Inverse artificial neural network for multiobjective antenna design,” *IEEE Trans. Antennas Propag.*, vol. 69, no. 10, pp. 6651–6659, 2021.

[10] T. McConaghay, P. Palmers, M. Steyaert, and G. G. E. Gielen, “Trustworthy genetic programming-based synthesis of analog circuit topologies using hierarchical domain-specific building blocks,” *IEEE Trans. Evol. Comput.*, vol. 15, no. 4, pp. 557–570, 2011.

[11] F. Azevedo, N. Lourenço, and R. Martins, “Comprehensive application of denoising diffusion probabilistic models towards the automation of analog integrated circuit sizing,” *Expert Syst. Appl.*, vol. 290, p. 128414, 2025.

[12] C. Liu, E. A. Olowe, and D. Chitnis, *LLM-based AI agent for sizing of analog and mixed signal circuit*, 2025. *arXiv: 2504.11497 [eess.SY]*.

[13] K. Settaluri, A. Haj-Ali, Q. Huang, K. Hakhamaneshi, and B. Nikolic, “Autockt: Deep reinforcement learning of analog circuit designs,” in *Proceedings of the 23rd Conference on Design, Automation and Test in Europe*, ser. DATE ’20, Grenoble, France: EDA Consortium, 2020, pp. 490–495.

[14] H. Wang, K. Wang, J. Yang, L. Shen, N. Sun, H.-S. Lee, and S. Han, “Gcn-rl circuit designer: Transferable transistor sizing with graph neural networks and reinforcement learning,” in *2020 57th ACM/IEEE Design Automation Conference (DAC)*, 2020, pp. 1–6.

[15] W. Lyu, P. Xue, F. Yang, C. Yan, Z. Hong, X. Zeng, and D. Zhou, “An efficient bayesian optimization approach for automated optimization of analog circuits,” *IEEE Transactions on Circuits and Systems I: Regular Papers*, vol. 65, no. 6, pp. 1954–1967, 2018.

[16] H. A. Wheeler, “The spherical coil as an inductor, shield, or antenna,” *Proceedings of the IRE*, vol. 46, no. 9, pp. 1595–1602, 1958.

[17] D. W. Knight, “Solenoid inductance calculation,” DW Knight, 2013.

[18] A. Mirhoseini, A. Goldie, M. Yazgan, J. W. Jiang, E. Songhori, S. Wang, Y.-J. Lee, E. Johnson, O. Pathak, A. Nova, J. Pak, A. Tong, K. Srinivasa, W. Hang, E. Tuncer, et al., “A graph placement methodology for fast chip design,” *Nature*, vol. 594, no. 7862, pp. 207–212, 2021.

[19] H. Chen, M. Liu, B. Xu, K. Zhu, X. Tang, S. Li, Y. Lin, N. Sun, and D. Z. Pan, “MAGICAL: An open-source fully automated analog IC layout system from netlist to GDSII,” *IEEE Design Test*, vol. 38, no. 2, pp. 19–26, 2021.

[20] Z. Dong, W. Cao, M. Zhang, D. Tao, Y. Chen, and X. Zhang, “CktGNN: Circuit graph neural network for electronic design automation,” in *The Eleventh International Conference on Learning Representations*, 2023.

[21] C.-C. Chang, Y. Shen, S. Fan, J. Li, S. Zhang, N. Cao, Y. Chen, and X. Zhang, “Lamagic: Language-model-based topology generation for analog integrated circuits,” *arXiv preprint arXiv:2407.18269*, 2024.

[22] Y. Lai, S. Lee, G. Chen, S. Poddar, M. Hu, D. Z. Pan, and P. Luo, “Analogcoder: Analog circuit design via training-free code generation,” in *Proceedings of the AAAI Conference on Artificial Intelligence*, vol. 39, 2025, pp. 379–387.

[23] W. Cao, M. Benosman, X. Zhang, and R. Ma, “Domain knowledge-based automated analog circuit design with deep reinforcement learning,” *arXiv preprint arXiv:2202.13185*, 2022.

[24] A. Mehradfar, X. Zhao, Y. Niu, S. Babakniya, M. Alesheikh, H. Aghasi, and S. Avestimehr, “AICircuit: A Multi-Level Dataset and Benchmark for AI-Driven Analog Integrated Circuit Design,” *Machine Learning and the Physical Sciences Workshop @ NeurIPS*, 2024.

[25] D. Krylov, P. Khajeh, J. Ouyang, T. Reeves, T. Liu, H. Ajmal, H. Aghasi, and R. Fox, “Learning to design analog circuits to meet threshold specifications,” in *Proceedings of the 40th International Conference on Machine Learning*, ser. ICML’23, Honolulu, Hawaii: JMLR.org, 2023.

[26] B. Liu, H. Zhang, X. Gao, Z. Kong, X. Tang, Y. Lin, R. Wang, and R. Huang, “Layoutcopilot: An ILM-powered multi-agent collaborative framework for interactive analog layout design,” *IEEE Transactions on Computer-Aided Design of Integrated Circuits and Systems*, 2025.

[27] Y. Li, Y. Lin, M. Madhusudan, A. Sharma, S. Sapatnekar, R. Harjani, and J. Hu, “A circuit attention network-based actor-critic learning approach to robust analog transistor sizing,” in *2021 ACM/IEEE 3rd Workshop on Machine Learning for CAD (MLCAD)*, 2021, pp. 1–6.